AD-A094 534 NAVAL RESEARCH LAB WASHINGTON DC F/G 12/1
THE NUMERICAL SOLUTION OF COUPLED NONLINEAR DIFFERENTIAL EQUATI--ETC(U)
JAN 81 P C WIGNEREY, R P MIED
UNCLASSIFIED NRL-MR-4448 NL

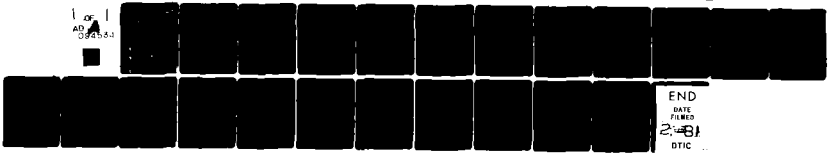

END
DATE FILMED
2-81
DTIC

NRL Memorandum Report 4534

The Numerical Solution of Coupled Nonlinear Differential Equations Occurring in Oceanographic Thermostad Modeling

PETER C. MCGREGOR and RICHARD P. MIED

Environmental Sciences Division

LEVEL II

28 Jan 81

23

January 28, 1981

RR011080

RR011080-43

NAVAL RESEARCH LABORATORY
Washington, D.C.

SECURITY CLASSIFICATION OF THIS PAGE (When Data Entered)

REPORT DOCUMENTATION PAGE		READ INSTRUCTIONS BEFORE COMPLETING FORM
1. REPORT NUMBER NRL Memorandum Report 4448	2. GOVT ACCESSION NO. AD-A094 534	3. RECIPIENT'S CATALOG NUMBER
4. TITLE (and Subtitle) THE NUMERICAL SOLUTION OF COUPLED NONLINEAR DIFFERENTIAL EQUATIONS OCCURRING IN OCEANOGRAPHIC THERMOSTAD MODELING		5. TYPE OF REPORT & PERIOD COVERED Interim report on a continuing NRL problem 6. PERFORMING ORG. REPORT NUMBER
7. AUTHOR(s) Peter C. Mignerey and Richard P. Mied		8. CONTRACT OR GRANT NUMBER(s)
9. PERFORMING ORGANIZATION NAME AND ADDRESS Naval Research Laboratory Washington, D.C. 20375		10. PROGRAM ELEMENT, PROJECT, TASK AREA & WORK UNIT NUMBERS 61153N, RR0110843 43-1139-0-1
11. CONTROLLING OFFICE NAME AND ADDRESS Naval Research Laboratory Washington, D.C. 20375		12. REPORT DATE January 28, 1981 13. NUMBER OF PAGES 22
14. MONITORING AGENCY NAME & ADDRESS(if different from Controlling Office)		15. SECURITY CLASS. (of this report) UNCLASSIFIED 15a. DECLASSIFICATION/DOWNGRADING SCHEDULE

16. DISTRIBUTION STATEMENT (of this Report)

Approved for public release; distribution unlimited.

17. DISTRIBUTION STATEMENT (of the abstract entered in Block 20, if different from Report)

18. SUPPLEMENTARY NOTES

19. KEY WORDS (Continue on reverse side if necessary and identify by block number)

Fine structure
Temperature profile
Thermostad
Mesoscale currents

20. ABSTRACT (Continue on reverse side if necessary and identify by block number)

A nonlinear numerical eigenvalue problem is solved to yield the shape and velocity profile of a submerged isothermal water mass assumed aximuthally symmetric and in gradient wind balance with a linearly stratified background. Solutions are found to exist and have widths ≳ 30 km, heights ≲ 100 m, and particle speeds at the rim ≲ 15 cm/sec.

DD FORM 1 JAN 73 1473 EDITION OF 1 NOV 65 IS OBSOLETE
S/N 0102-014-6601

SECURITY CLASSIFICATION OF THIS PAGE (When Data Entered)

CONTENTS

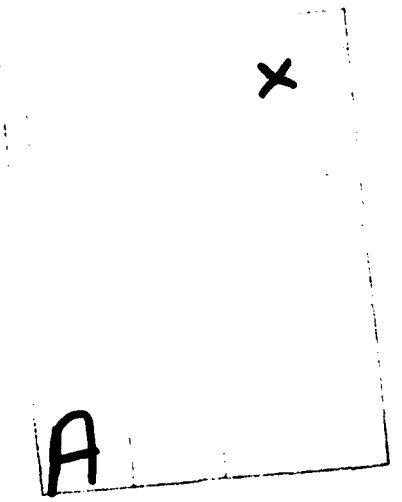

THE NUMERICAL SOLUTION OF COUPLED NONLINEAR DIFFERENTIAL EQUATIONS OCCURRING IN OCEANOGRAPHIC THERMOSTAD MODELING

I. INTRODUCTION

Traces of temperature as a function of depth show evidence of isothermal masses of water (thermostads) embedded in an otherwise stratified ocean. These thermostads generally reside at depths of 400-1000 m, have thicknesses of approximately 100 m, and diameters no greater than 50 km (see also Broome, Teague, and Hallock, 1979, and Rossby, 1980). To our knowledge, no theoretical work has been done to model their shape and velocity fields; although, two recent Gulf Stream ring papers are of related interest.

Csanady (1979) has constructed a two-layer model of warm core rings employing conservation of potential vorticity and radial momentum. Flierl (1979) then expanded this work by including the cyclostrophic term [(azimuthal velocity)^2/radius] which arises in the transformation to circular coordinates. These principles are also incorporated in this work. We model the thermostad as an oblate oval solid of constant density water (Fig. 1) which rotates anticyclonically relative to a stationary ocean having a linear density stratification. We then seek steady, axisymetric solutions to the inviscid equations of motion within the region of constant density, and ignore the β effect because of the small size of the thermostad. The equilibrium shape then results from a balance between the pressure gradient, Coriolis and cyclostrophic forces.

Manuscript submitted on December 10, 1980.

II. EQUATIONS OF MOTION

The inviscid Navier-Stokes and continuity equations in a rotating cylinderical coordinate system, as simplified by the assumption of steady, axisymetric flow inside the region of constant density (ρ_0) are:

$$\frac{v^2}{r} + fv = \frac{1}{\rho_0} P_r \tag{1}$$

$$fu = 0 \tag{2}$$

$$P_z = -\rho_0 g \tag{3}$$

$$v = v(r) \tag{4}$$

where (u, v) are the velocities in the (r, θ) directions and z is positive upwards. The existence of Taylor columns can be shown by adding the quantities $\frac{\partial}{\partial z}$ (1) and $\frac{\partial}{\partial r}$ (3). Then $\left(\frac{2v}{r} + f\right) v_z = -\frac{1}{\rho_0} P_{rz} = 0$ which proves that v is independent of z. The most natural way to remove the degeneracy of (2) and (4) is to introduce the principle of conservation of potential vorticity, that is

$$\frac{\omega + f}{L} = \text{constant} \tag{5}$$

where

$$\omega = \frac{1}{r}\left(\frac{\partial}{\partial r}(rv) - \frac{1}{r}\frac{\partial u}{\partial \theta}\right) \tag{6}$$

is the relative vorticity, f the Coriolis parameter, and L the length of a Taylor column.

To obtain a pair of equations for the velocity and column height it is necessary to express the radial pressure gradient $\frac{\partial P}{\partial r}$ in terms of the column height. Taking advantage of the vertical symmetry of the oval about a horizontal plane, we introduce the half-height $|h| \equiv L/2$ so that $\pm h(r)$ defines the surface of the thermostad. Since the external pressure field of the ocean is known, it is possible to find the pressure at $h(r)$. The vertical pressure gradient in a linearly stratified ocean is

$$\frac{\partial P}{\partial z} = -\rho_0 g\ (1 - \delta z).$$

The pressure may be obtained by integrating once:

$$P(z) = -\rho_0 g\ (z - 1/2\, \delta z^2) + P_0$$

where P_0 is a reference pressure at $z = 0$. Likewise, the pressure field inside the thermostad is

$$P(r,z) = -\rho_0 gz + c(r).$$

Both pressure fields must match over the entire surface of the thermostad

$$P(h(r)) = -\rho_0 g\ (h - 1/2\,\delta h^2) + P_0 = -\rho_0 gh + c(r)$$

so that

$$c(r) = 1/2\,\rho_0 g\delta h^2 + P_0.$$

Hence, inside the thermostad

$$\frac{\partial P}{\partial r} = 1/2\,\rho_0 g\delta\ \frac{\partial |h^2|}{\partial r}. \tag{7}$$

Substitution of (7) into (1) produces

$$\frac{v^2}{r} + fv = \frac{1}{2}\ g\delta\ \frac{dh^2}{dr}. \tag{8}$$

We now have h and v in a single nonlinear equation. Another equation may be obtained from (5) and (6):

$$\frac{dv}{dr} + \frac{v}{r} = f\left(\frac{|h|}{H_0} - 1\right), \tag{9}$$

where $2H_0$ is the length to which a Taylor column must be stretched to bring the relative vorticity to zero.* We look for a family of solutions corresponding to columns which have contracted, causing a negative relative vorticity. For $h \approx H_0$ there is very little contraction and only a small amount of relative vorticity. In the opposite extreme ($h << H_0$), the contraction is large, as is the relative vorticity. The boundary conditions for (8,9) are

$$v(0) = 0, \tag{10}$$

$$h(r_0) = 0. \tag{11}$$

where r_0 is the radius of the thermostad.

Equations (8,9) with boundary conditions (10,11) are nondimensionalized by letting

$$r = R\hat{r}, \qquad v = V_0\hat{v}, \qquad h = H_0\,\hat{h} \tag{12}$$

*It will emerge in Section VII that all observed solutions are clustered around $h(0) \approx H_0$. In effect, then, $2H_0$ is very nearly the thermostad height.

so that

$$\epsilon^2 \frac{\hat{v}^2}{\hat{r}} + \epsilon \hat{v} = \frac{1}{2} \frac{d\hat{h}^2}{d\hat{r}} \tag{13}$$

$$\epsilon \left[\frac{d\hat{v}}{d\hat{r}} + \frac{\hat{v}}{\hat{r}} \right] = |\hat{h}| - 1 \tag{14}$$

$$\tilde{v}(0) = 0, \tag{15}$$

$$\hat{h}\ (\hat{r}_0) = 0 \tag{16}$$

where $\epsilon \equiv \frac{V_0}{Rf}$ is the Rossby number and $R = \frac{H_0}{f}\ (g\delta)^{1/2} = \frac{H_0 N}{f}$ is the radius of deformation. Since the velocity scale is chosen as the velocity at the edge,

$$\hat{v}\ (\hat{r}_0) = 1 \text{ and } V_0 = \epsilon N H_0; \tag{17}$$

then the nondimensionalization (12) takes the form:

$$r = \frac{N}{f} H_0\, \hat{r},\ v = \epsilon N H_0\, \hat{v},\ h = H_0 \hat{h}. \tag{18}$$

The system of Eqs. (13-16) constitute an eigenvalue probelm for ϵ. Because ϵ and $\hat{v}$ consistently occur in each equation only as a product, the eigenvalue problem is greatly simplified. After introducing the change of variables $\tilde{v} \equiv \epsilon \hat{v}$ the following initial value problem is solved:

$$\frac{\tilde{v}^2}{\hat{r}} + \tilde{v} = 1/2 \frac{d\hat{h}^2}{dr} \tag{19}$$

$$\frac{d\tilde{v}}{d\hat{r}} + \frac{\tilde{v}}{\hat{r}} = |\hat{h}| - 1 \tag{20}$$

$$\tilde{v}(0) = 0 \tag{21}$$

$$0 < \hat{h}(0) < 1. \tag{22}$$

These equations are integrated beginning at the origin and continuing until $\hat{h}(r) = 0$. This determines $\hat{r}_0$ and $\tilde{v}(r_0)$. The corresponding eigenvalue is then given by $\epsilon = |\tilde{v}(\hat{r}_0)|$. Each initial value $\hat{h}(0)$ is thus uniquely related to a particular $\hat{r}_0$ and ϵ.

III. PROPERTIES OF THE SOLUTION

The system (19-22) has been solved in detail on the computer. However certain properties may be deduced using analysis. Since both (19) and (20) are even in h, the surface of the thermostad is indeed symmetric about $z = 0$. Furthermore at $r = r_0$ we expect the pressure gradient $\hat{h} \frac{d\hat{h}}{d\hat{r}}$ to be

bounded. Since $\hat{h}(\hat{r}_0) = 0$ we anticipate $\frac{d\hat{h}}{d\hat{r}} \to \infty$; the solutions support this. Below, we obtain the shape in the limiting case $h(0) << 1$, and derive the properties of the thermostad for all $\hat{h}(0)$ in the vicinity of $\hat{r} = 0$.

A. Solution for $\hat{h}(0) << 1$

An analytic solution may be obtained for (19-22) in the limit $h \to 0$. Then (20) becomes

$$\frac{d\tilde{v}}{d\hat{r}} + \frac{\tilde{v}}{\hat{r}} \simeq -1,$$

which has the solution

$$\tilde{v} = -\hat{r}/2 + \frac{c_1}{\hat{r}}.$$

The initial condition (21) forces $c_1 = 0$ and

$$\tilde{v}(\hat{r}) = -\hat{r}/2. \tag{23}$$

Using this expression in (19), we see that

$$\frac{d\hat{h}^2}{d\hat{r}} = -\frac{1}{2}\hat{r}^2 \tag{24}$$

or

$$\hat{h}^2(\hat{r}) = -\frac{1}{4}\hat{r}^2 + c_2.$$

At the outer edge of the thermostad, $\hat{r} = \hat{r}_0$ and $\hat{h} = 0$; thus $c_2 = \frac{1}{4}\hat{r}_0^2$ and

$$\hat{h}(\hat{r}) = \frac{1}{2}\sqrt{\hat{r}_0^2 - \hat{r}^2}. \tag{25}$$

The surface is thus given by $4\hat{h}^2 + \hat{r}^2 = \hat{r}_0^2$ which shows the thermostad to be an *oblate ellipsoid* with $\hat{r}_0 = 2\hat{h}(0)$. Furthermore, differentiation of (25) verifies the conjecture $\left.\frac{d\hat{h}}{d\hat{r}}\right|_{\hat{r}=\hat{r}_0} \to \infty$. However (24) shows that $\frac{d\hat{h}^2}{d\hat{r}}$ is finite at $\hat{r}_0$. Although we have only shown that $|\hat{h}\frac{d\hat{h}}{dr}| < \infty$ for $\hat{h}(0) << 1$, the numerical solutions of section IV support the veracity of this assertion for all $\hat{h}(0)$.

B. Power Series Solution Near $\hat{r} = 0$

An analytic solution near the origin is needed for a successful implementation of the computer solution in the following section. For small r the power series expansions

$$\tilde{v}(\hat{r}) = \sum_{n=0}^{\infty} \tilde{v}_n \hat{r}^n$$

and

$$\hat{h}(\hat{r}) = \sum_{n=0}^{\infty} \hat{h}_n \hat{r}^n$$

are introduced into (19) and (20). We may then group the terms according to orders of $\hat{r}$.

$$0\left(\frac{1}{\hat{r}}\right): \quad \tilde{v}_0^2 = 0, \qquad \tilde{v}_0 = 0 \tag{26a,b}$$

$$0(1): \quad 2\tilde{v}_0\tilde{v}_1 + \tilde{v}_0 = \hat{h}_0\hat{h}_1, \qquad 2\tilde{v}_1 = \hat{h}_0 - 1 \tag{27a,b}$$

$$0(\hat{r}): \quad 2\tilde{v}_0\tilde{v}_2 + \tilde{v}_1^2 + \tilde{v}_1 = 2\hat{h}_0\hat{h}_2 + \hat{h}_1^2, \qquad 3\tilde{v}_2 = \hat{h}_1. \tag{28a,b}$$

The importance of these equations lies in the implications to be drawn from the 0(1) terms. Since $\tilde{v}_0 = 0$ and $\hat{h}_0 \neq 0$, Eq. (27a) implies $\hat{h}_1 = 0$ and (27b) yields $\tilde{v}_1 = \dfrac{\hat{h}_0 - 1}{2}$ while (28b) gives $\tilde{v}_2 = 0$. Thus, for small $\hat{r}_1$ we may write

$$\tilde{v}(\hat{r}) = \left(\frac{\hat{h}_0 - 1}{2}\right)\hat{r} + 0\,(\hat{r}^3) \tag{29}$$

and

$$\hat{h}(\hat{r}) = \hat{h}_0 + 0(\hat{r}^2). \tag{30}$$

We employ (29) and (30) in the computer solution below.

IV. COMPUTER SOLUTION

Equations (19) and (20) are a pair of first order nonlinear differential equations which may be rewritten as:

$$\frac{d\hat{g}}{d\hat{r}} = \frac{\tilde{v}^2}{\hat{r}} + \tilde{v} \tag{31}$$

$$\frac{d\hat{v}}{d\hat{r}} = \sqrt{2\hat{g}} - 1 - \frac{\tilde{v}}{\hat{r}} \tag{32}$$

where

$$\hat{g} \equiv \frac{1}{2}\,\hat{h}^2.$$

Two advantages accrue from this change of variables. Near the edge of the thermostad $\frac{d\hat{g}}{d\hat{r}}$ is well-behaved, and any standard scheme for solving a well-behaved first order system can be used.* We have written a subroutine called DIFF (see Appendix A) which evaluates (31) and (32) in a form usable by the integration procedure DIFSYS. Two minor problems arise. The integration procedure begins at the origin where the $1/r$ terms in (31) and (32) are infinite. In order to begin the integration, we employ the power series solution (28,29) at $\hat{r} = 0$ to obtain $\left.\frac{d\hat{g}}{d\hat{r}}\right|_0 = 0$ and $\left.\frac{d\tilde{v}}{d\hat{r}}\right|_0 = \frac{\sqrt{2\hat{g}_0} - 1}{2}$.

The other problem occurs at the edge of the thermostad. Resolution of the radius $\hat{r}_0$ is no better than the step size $\Delta\hat{r}$. On the other hand, the choice of a small $\Delta\hat{r}$ would increase the computer time prohibitively. Fortunately the accuracy of DIFSYS is of order $(\Delta\hat{r})^2$ (Bulirsch and Stoer 1966 b), so that a small $\Delta\hat{r}$ is not needed to maintain accuracy of $\hat{h}$ and $\tilde{v}$. Hence, a large $\Delta\hat{r}$ is used until the edge is detected (i.e., when $\hat{g}$ becomes negative). At this point the subroutines backtrack to the last known point having $\hat{g} > 0$. $\Delta\hat{r}$ is then divided by ten and the integration proceeds in this manner until $\Delta\hat{r}$ is less than the convergence tolerance. The evaluation of $\hat{r}_0$ is then considered to be finished.

Although the overall accuracy of the method is $0[(\Delta r)^2]$, a few sample calculations were made to ensure the proper choice of Δr. The results summarized in Table 1 indicate a value of $\Delta\hat{r} = 10^{-2}$ is

Table 1
Values for $\hat{h}(\hat{r})$ and $\tilde{v}(\hat{r})$ at $\hat{r} = 1$
for various values of $\Delta\hat{r}$.

$\Delta\hat{r}$	$\hat{h}(1)$	$\tilde{v}(1)$	# of computations
10^{-1}	.22369	−.30885	10
10^{-2}	.22357	−.30886	100
10^{-3}	.22256	−.30897	1000

*In this paper we use the routine DIFSYS which is available through the NRL Research Computation Division. It is an extrapolation method based upon the works of Bulirsch and Stoer (1966 a,b).

appropriate for three place accuracy in $\hat{h}$ and $\tilde{v}$. The smaller value requires too many calculations and the larger value produces too few data points. Accordingly the convergence tolerance for $\Delta\hat{r}$ was chosen to be 10^{-3}.

V. NUMERICAL RESULTS

The functions $\hat{h}(\hat{r})$, $\tilde{v}(\hat{r})$ and the radius $\hat{r}_0$ were computed for values of $\hat{h}(0) = .05, .10, \cdots .90, .95, 1.00, 1.05$. The results are summarized in Figs. 2 and 3. Figure 2 shows $\hat{h}(\hat{r})$ for several values of $\hat{h}(0)$; these curves correspond to different values of ϵ. Closed surfaces exist when $\hat{h}(0) < 1$; note that no such surface exists for the curves $\hat{h}(0) = 1.00, 1.05$. The associated velocity field (Fig. 3) is negative and monotonically increasing in magnitude more rapidly than a linear function of $\hat{r}$. Although the radial velocity gradient is larger for small $\hat{h}(0)$, the large size of $\hat{r}_0$ for large $\hat{h}(0)$ produces a larger peak velocity.

For small values of $\epsilon \left(= \frac{V_0}{NH_0}\right)$ the computer solutions approach the asymptotic solutions (23) and (25). In particular, the aspect ratio $\alpha \equiv \hat{h}(0)/\hat{r}_0 = \frac{Nh(0)}{fr_0}$ approaches 0.5, as shown in Fig. 4. For larger values of ϵ the aspect ratio is smaller, which indicates the thermostad is more oblate when the fluid has less relative vorticity. This raises the question as to how much the function $\hat{h}(\hat{r})$ deviates from the ellipsoidal limit ($\epsilon \approx 0$) when ϵ, $\hat{h}(0)$ and $\hat{r}_0$ assume larger values. To answer this, the variables were normalized as follows:

$$r^* = \hat{r}/\hat{r}_0, \; h^*/\hat{h}(0), \; v^* = \tilde{v}/\tilde{v}(\hat{r}_0).$$

As a result of this normalization, all thermostads transform to shapes with unit radius and unit height. Some normalized thermostads are shown in Figs. 5 and 6 for two different values of ϵ. For the larger value of ϵ the surface of the thermostad is more square than elliptical, and the velocity is markedly nonlinear.

As indicated above, two pathological cases were run. For $\hat{h}(0) = 1.00$ the Taylor columns exist at their initial (pre-collapse) height; thus there is no relative vorticity. Hence the velocity is zero every-

where and the bounding thermostad surface extends to infinity. When $\hat{h}(0) > 1$, e.g., $\hat{h}(0) = 1.05$, the Taylor columns are stretched producing positive relative vorticity and corresponding positive (cyclonic) velocities. The surface is again unbounded as it rises away from the origin.

VI. A METHOD FOR OBTAINING THE ROSSBY NUMBER AND HEIGHT SCALE

The shape and velocity field of a thermostad depend on the value of ϵ. However ϵ is not easy to determine for a dimensional thermostad even if $v(r_0)$ is known. This is because the scale height H_0 appears in all of the nondimensionalizations (18), and H_0 is not directly measureable for a thermostad in the ocean. Two measurements which are less difficult to make are $h(0)$ and r_0. Since each of these quantities depends on the Rossby number, the aspect ratio α $(= \hat{h}(0)/\hat{r}_0)$ is also a function of ϵ, $\alpha = \alpha(\epsilon)$. This functional dependence is shown in Fig. 4. From the nondimensionalization (18), we may express α as $\alpha = \frac{N}{f}\frac{h(0)}{r_0}$. Since the depth $h(0)$ and radius r_0 can be estimated from the data, ϵ may be found for and observed thermostad. Then the height scale is given by $H_0 = h(0)/\hat{h}(0;\epsilon)$ where $\hat{h}(0;\epsilon)$ is shown in Fig 7a; the results for $\hat{r}_0$ as a function of ϵ are shown in Fig. 7b. With ϵ and H_0 thus obtained, Figs. 2 and 3 and the scaling (18) may be used to estimate the shape and velocity field in dimensional form.

One further problem occurs when the data is reduced. The radius r_0 is not precisely known; only an upper bound can be established by examining contiguous XBT's. This leads to inequalities for α, ϵ, H_0 and V_0. In trying to establish the inequality for V_0, Eq. (17) is needed. Unfortunately the inequalities are such that ϵ is less than some bound and H_0 greater than another bound, leaving the product indeterminate. Likewise $\hat{h}(0;\epsilon) = h(0)/H_0$ implies $\hat{h}(0;\epsilon)$ is less than a bound. To avoid this problem, a velocity/height ratio is introduced, $\beta \equiv \frac{\epsilon}{\hat{h}(0;\epsilon)} = \frac{V_0}{Nh(0)}$ (33). This ratio, which is a function of ϵ, is shown in Fig. 8. The slope of this curve in conjunction with the inequality for ϵ implies β is greater than a bound. Likewise the equation $V_0 = \beta N h(0)$ means the peak velocity can only be esitmated as exceeding some minimum value.

VII. APPLICATION TO OBSERVED THERMOSTADS

Traces of temperature as a function of depth, obtained by several XBT's, show evidence of thermostads (Figs. 9a-g). Aside from Figs. 9d and 9f, however, there is only a single trace through any of the suspected thermostads. In no case is a velocity measurement available; consequently, an estimate of the aspect ratio $\alpha\left[=\frac{N}{f}\frac{h(0)}{r_0}\right]$, peak velocity $v(r_0)$ and height scale $h(0)$ is all that can be obtained. To accomplish this, the Brunt-Väisälä frequency must be evaluated. Based on historical temperature-salinity data corresponding to the location of the XBT, the salinity and σ_T are computed as a function of depth. The Brunt-Väisälä frequency is then obtained using the central difference formula $N^2 = \frac{g}{\rho_0}\left[\frac{\rho_+ - \rho_-}{z_+ - z_-}\right]$ at depth $z = z_0$. Since differentiation produces varying results due to fluctuations in the data, we formed two averages for N: one actually within the thermostad, and the other over the surrounding neighborhood.

The local value for f was found using the known latitude of the XBT. The vertical location of the thermostad was obtained by drawing a straight line through the thermostad and subjectively determining where the temperature gradient changes slope. Then the thickness was measured from the plot and halved to form $h(0)$. Because of the sparseness of the data, only an upper bound can be set for r_0 based on the distance between contiguous XBT's. Using the data in conjunction with the theory allows bounds to be put on ϵ, α, H_0 and V_0.

As summarized in Table 2, the observed thermostads are oblate, having an aspect ratio in the range $.119 \leqslant \alpha \leqslant .182$. This low value of α is due to the thinness of the observed mass of water in conjunction with the large upper bound on the diameter. Although the thermostads are thin, the heights of their Taylor columns are not much less than the scale height. Indeed, $\hat{h}(0)$ which is a measure of this contraction is in the range .992 to .999. A significant result of this work is H_0 approximately equals half the thermostad height, with less than 1% error.

Table 2
A Comparison of the Observed Parameters and Derived Inequalities for Several Thermostads

Figure	9a	9b	9c	9d	9e	9f	9g
r_0 (km) $\leqslant$	26	22	26	27	28	32	25
$h(0)$ (m) =	97	65	65	85	100	47	52
$N_{outside}\left(\frac{rad}{s}\right)$ =	$.385 \cdot 10^{-2}$	$.366 \cdot 10^{-2}$	$.403 \cdot 10^{-2}$	$.373 \cdot 10^{-2}$	$.407 \cdot 10^{-2}$	$.430 \cdot 10^{-2}$	$.379 \cdot 10^{-2}$
$N_{inside}\left(\frac{rad}{s}\right)$ =	$.310 \cdot 10^{-2}$	$.190 \cdot 10^{-2}$	$.124 \cdot 10^{-2}$	$.093 \cdot 10^{-2}$	$.244 \cdot 10^{-2}$	$.324 \cdot 10^{-2}$	$.317 \cdot 10^{-2}$
$f\left(\frac{rad}{s}\right)$ =	$.862 \cdot 10^{-4}$	$.885 \cdot 10^{-4}$	$.834 \cdot 10^{-4}$	$.794 \cdot 10^{-4}$	$.800 \cdot 10^{-4}$	$.899 \cdot 10^{-4}$	$.876 \cdot 10^{-4}$
$\alpha \geqslant$	.167	.122	.121	.148	.182	.070	.090
$\epsilon \leqslant$	.553	.561	.561	.557	.551	.566	.565
$\beta \geqslant$	.559	.561	.561	.560	.559	.566	.565
$\gamma_0 <$	6.04	8.232	8.232	6.930	5.472	11.294	10.680
$h_0 <$	.992	.999	.999	.995	.987	.9999	.9999
H_0 (m) $\geqslant$	97.8	65.1	65.1	85.4	101.3	47	52
V_0 (m/s) $\geqslant$	.209	.133	.147	.178	.228	.114	.111

The observed thermostads appear to have a weak relative vorticity. The Rossby number which is obtained from Fig. 4 once α is known lies in the interval .551 to .561 and is large enough for significant departures from geostrophic flow to occur. An estimate of the peak velocity may be obtained using (33). Based on the bounds for ϵ, Fig. 8 is used to obtain β, which lies in the range .559 to .562. The associated peak velocities are then .132 (m/s) to .228 (m/s). Although these velocities are large, we believe they are reasonable in view of the theory's neglect of a Brunt-Väisälä frequency inside the thermostad (see Table 2). An inclusion of non-constant $N(z)$ would lead to smaller velocities.

Clearly, a measurement of the velocity field inside a thermostad would be a more stringent test of the theory. Unfortunately such measurements may be difficult to make. A more fruitful approach would entail dropping a sufficient number of XBT's to enable a comparison of the predicted and observed shapes, along with a better determination of r_0.

ACKNOWLEDGMENTS

The authors gratefully acknowledge the assistance of J. P. Dugan and A. F. Schuetz of the Naval Research Laboratory for allowing the use of their XBT traces (Fig. 9a-g).

REFERENCES

1. Broome, R.D., W.J. Teague, and Z.R. Hallock, Observation of an anticyclonic mid-ocean eddy with a deep homogeneous layer. *Trans. Am. Geophys. Un. (EOS)* **60**, 46, 862-863.

2. Bulirsch, R. and J. Stoer: Numerical Treatment of Differential Equations by Extrapolation Methods, *Numerische Mathematik* **8**, pp. 1-13 (1966a).

3. Bulirsch, R. and J. Stoer: Asymptotic Upper and Lower Bounds for results of Extrapolation Methods, Numerische Mathematik **8**, pp. 93-104 (1966b).

4. Csanady, G.T.: The birth and death of a warm core ring, *J. Geophys. Res.* **84** C2, 777-780 (1979).

5. Flierl, G.R.: A Simple Model for the Structure of Warm and Cold Core Rings, *J. Geophys. Res* **84**, pp. 781-785 (1979).

6. Pedlosky, J.: Geophysical Fluid Dynamics. *Mathematical Problems in the Geophysical Sciences*, Vol. 1. W.H. Reid, Ed. published by *Am. Math. Soc.* 1-60.

7. Rossby H.T., On the structure and origin of a small lens of water trapped in the main thermocline. Unpublished manuscript in *Polymode News* **76**, 4 (1980).

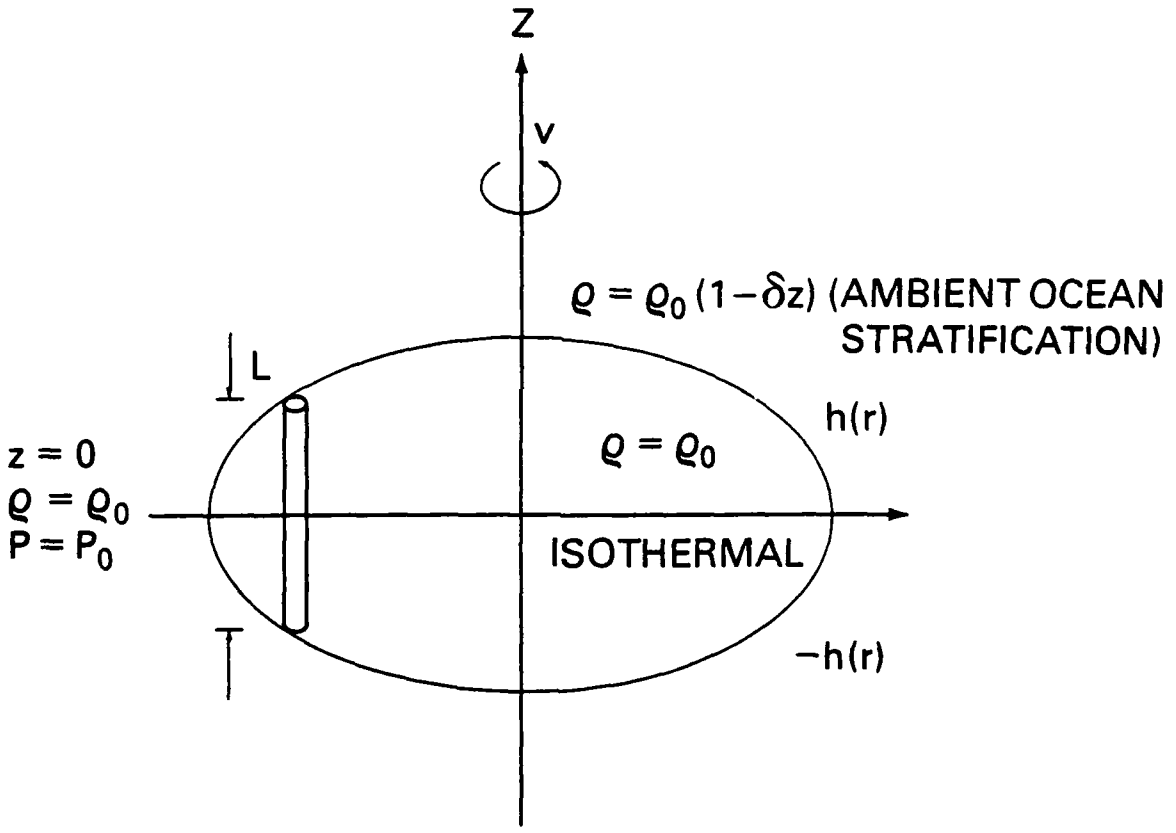

Fig. 1. — A constant-density thermostad embedded in a linearly stratified ocean has Taylor columns of length L, shape $h(r)$ and a velocity distribution $v(r)$

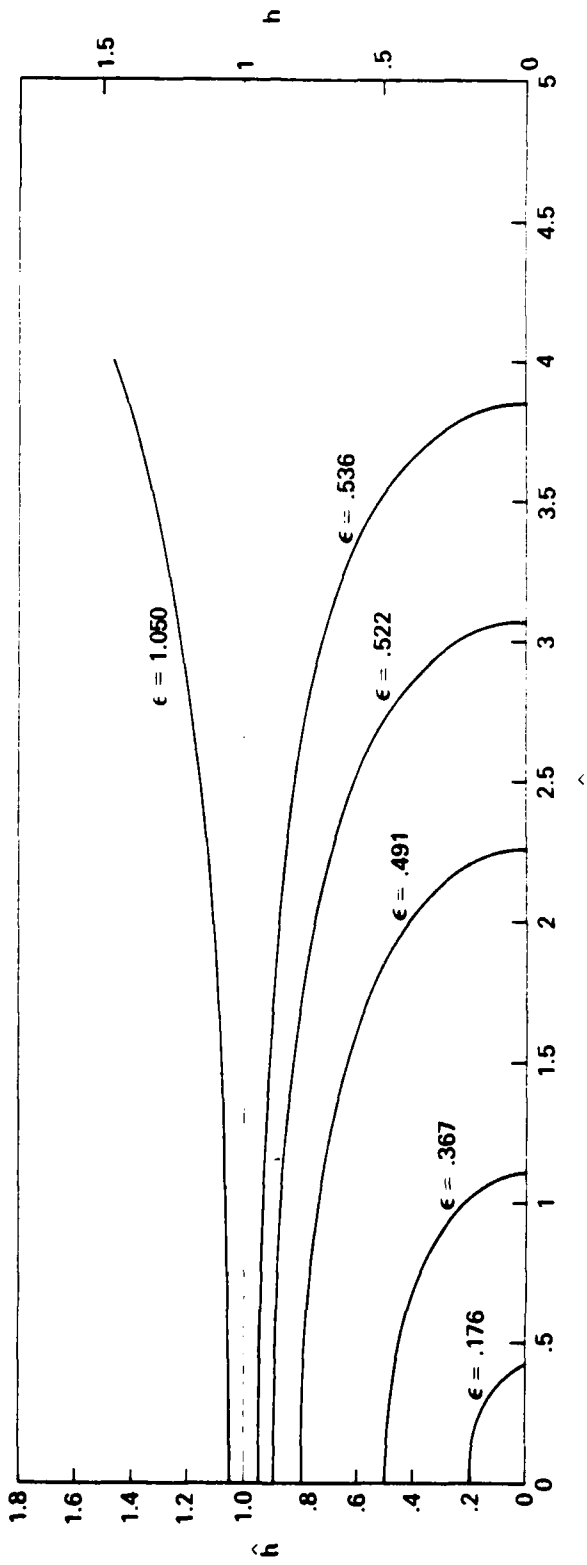

Fig. 2 — Thermostad shapes $\hat{h}\left[=h/H_0\right]$ as a function of $\hat{r}\left[=\frac{fr}{NH_0}\right]$ for different $\epsilon\left[=\frac{V_0}{NH_0}\right]$

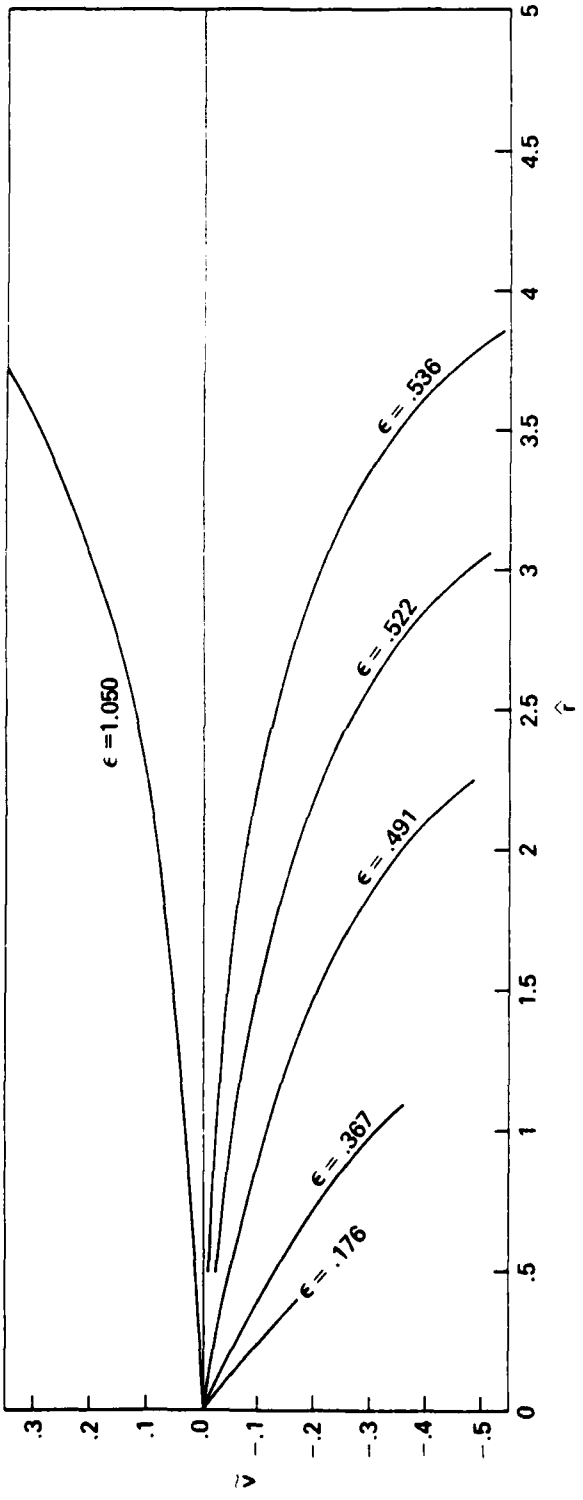

Fig. 3 — Azimuthal velocity $\tilde{v}\left[=\frac{v}{NH_0}\right]$ as a function of $\hat{r}\left[=\frac{fr}{NH_0}\right]$ for different $\epsilon\left[=\frac{v_0}{NH_0}\right]$

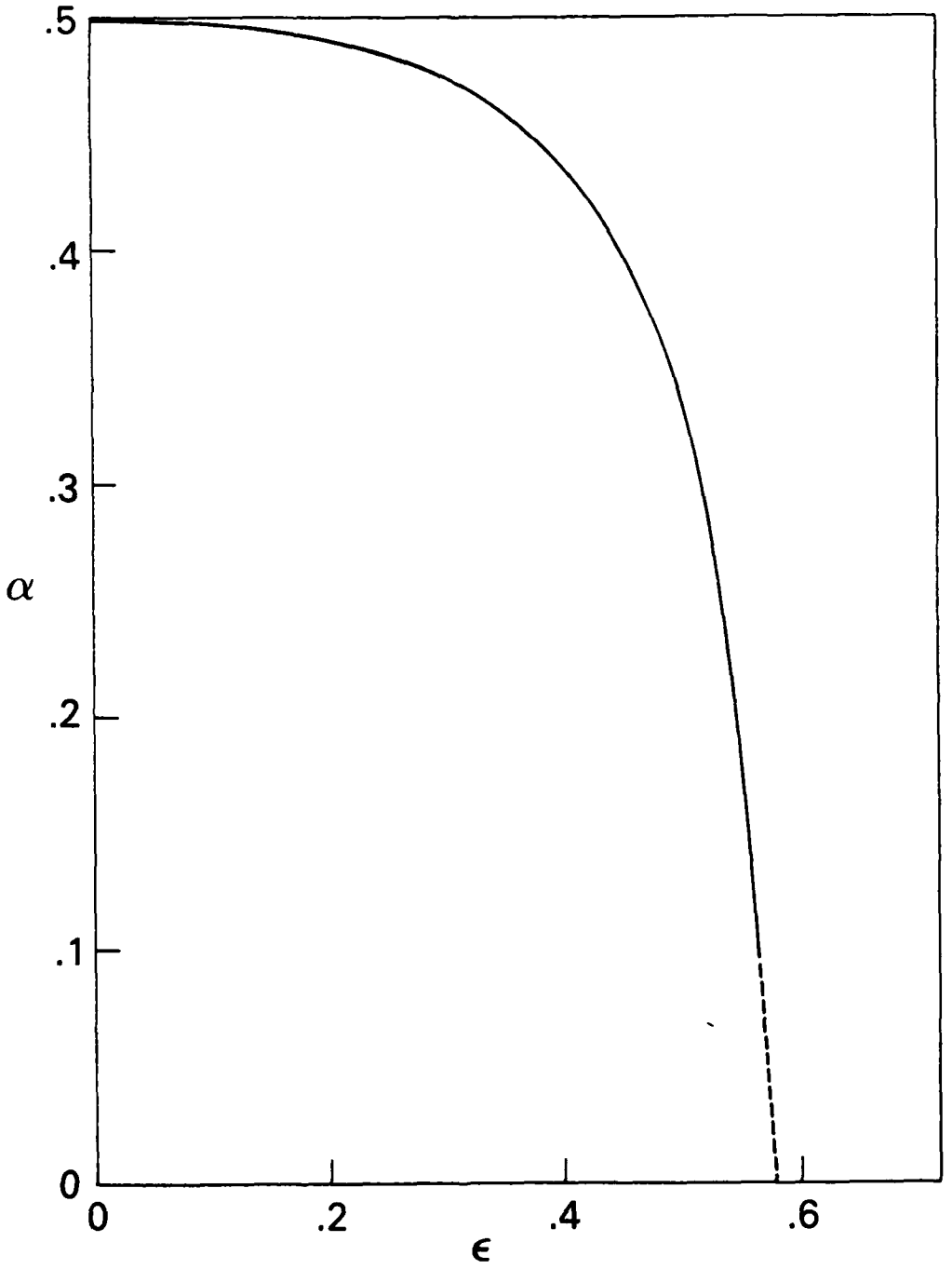

Fig. 4 — Aspect ratio $\alpha \left[= \frac{N}{F} \frac{h(0)}{r_0}\right]$ as a function of Rossby number $\epsilon \left[= \frac{V_0}{NH_0}\right]$. The limiting case $\epsilon \to 0$ is discussed in Section III A.

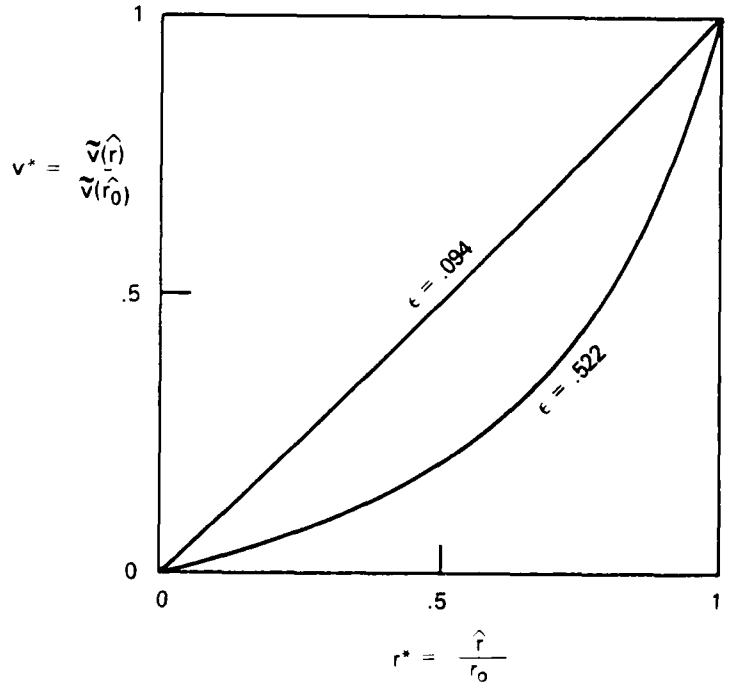

Fig. 5 — $\tilde{v}(\hat{r})$, renormalized with $\tilde{v}(\hat{r}_0)$ indicates that different values of $\epsilon \left[= \frac{v_0}{NH_0}\right]$ yield very different velocity profiles

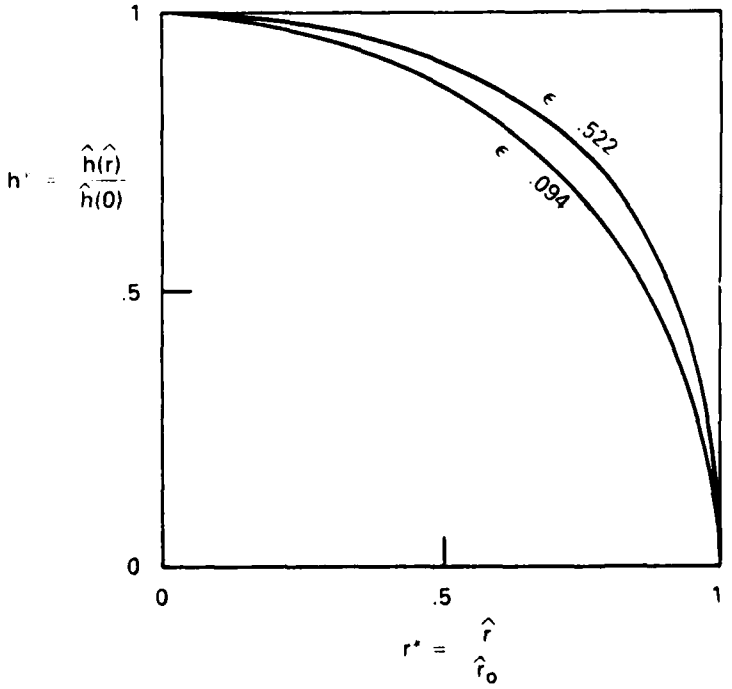

Fig. 6 — Same as 5, but showing $\hat{h}(\hat{r})/\hat{h}(0)$

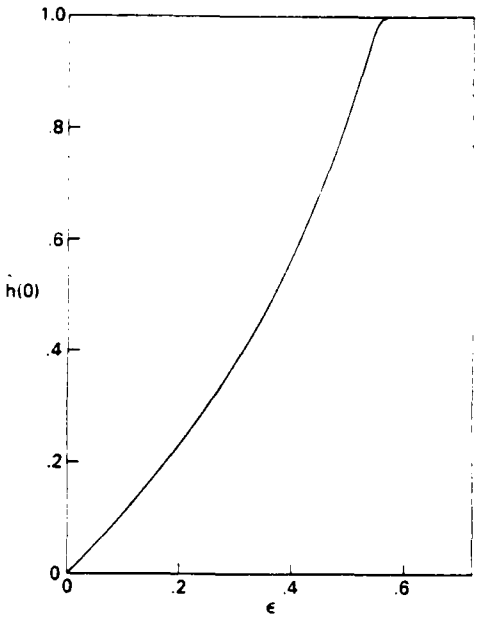

Fig. 7a — Variation of the initial height $\hat{h}(0)$ $\left[=\frac{h(0)}{H_0}\right]$ as a function of ϵ $\left[=\frac{V_0}{NH_0}\right]$

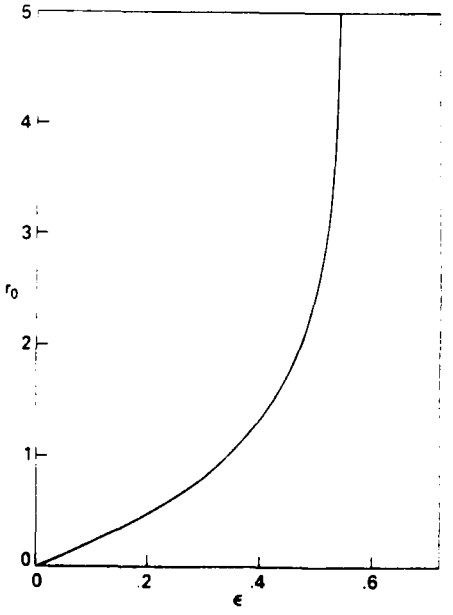

Fig. 7b — Variation of maximum radius $\hat{r}_0$ $\left[=\frac{fr_0}{HN_0}\right]$ as a function of Rossby number ϵ $\left[=\frac{V_0}{NH_0}\right]$. Note that the limiting value (max ϵ) = 0.58.

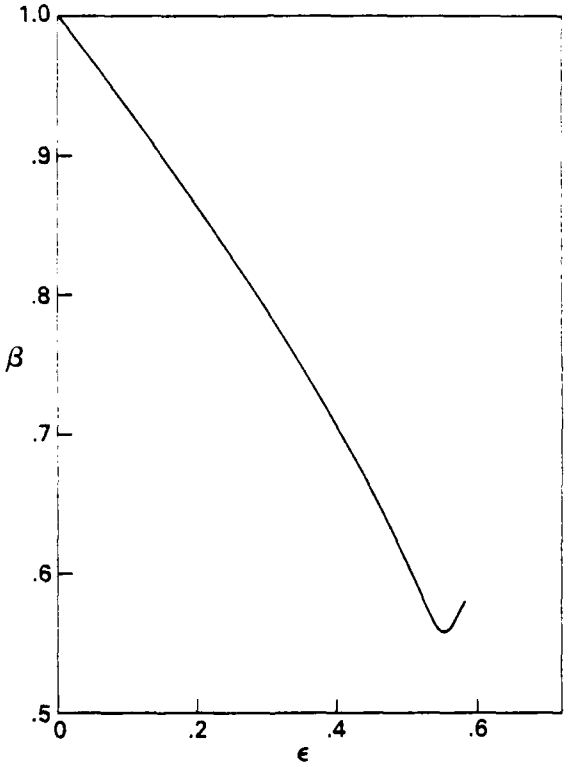

Fig. 8 — β [= $V_0/Nh(0)$] plotted as a function of $\epsilon \left[= \frac{V_0}{NH_0} \right]$

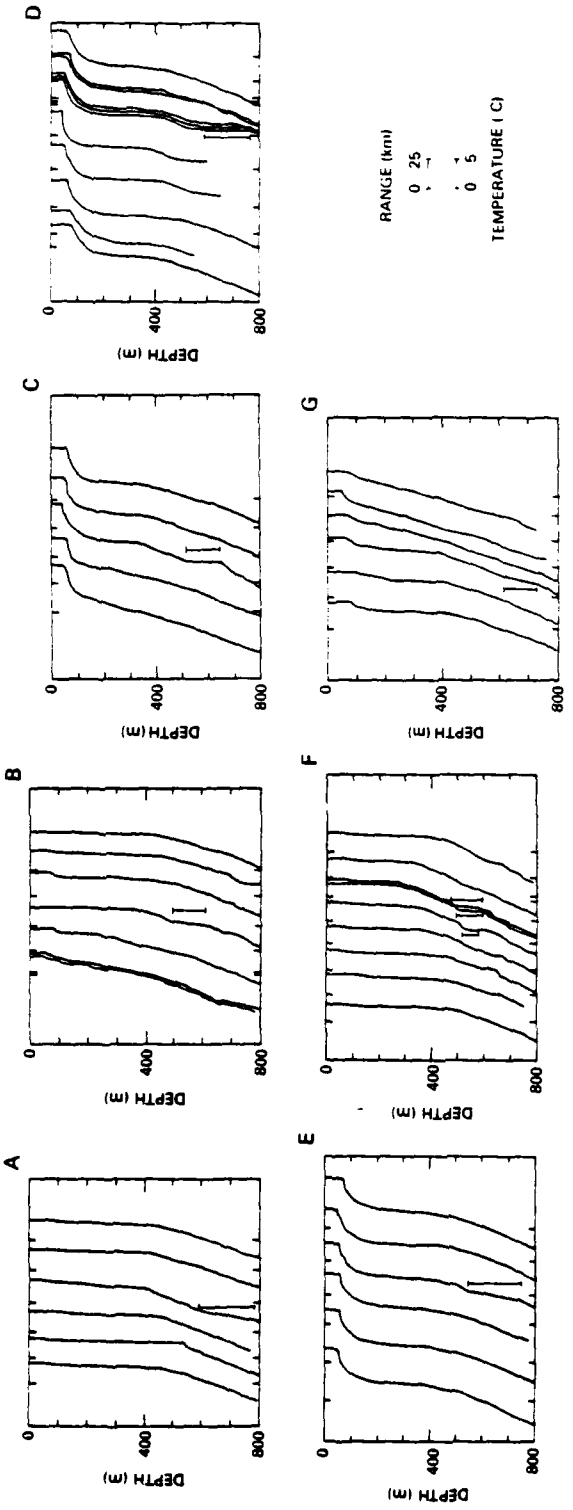

Fig. 9a-g — Actual temperature traces obtained from XBT's. The regions of suspected thermostads are marked with a vertical line which links two horizontal lines. Note that the thermostads appear on contiguous casts only in Figs. 9d and f.

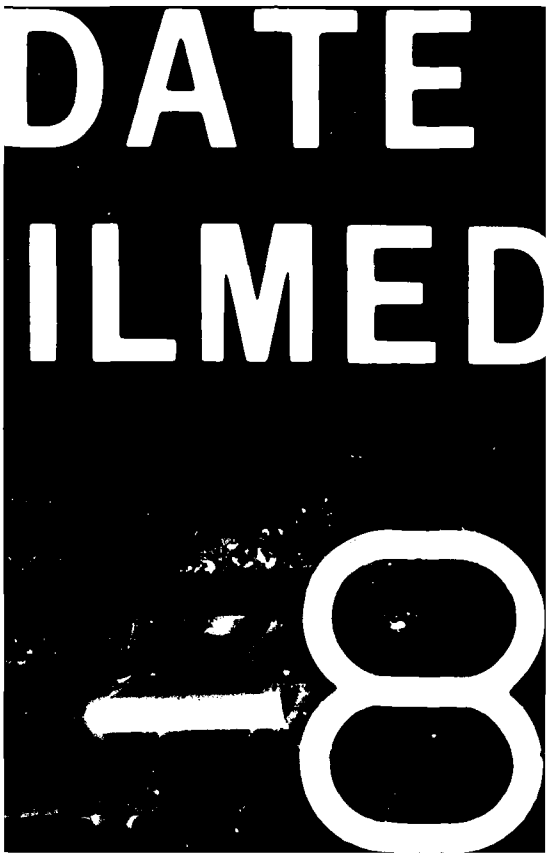
DATE
ILMED
8